Incipient space weathering on asteroid 162173 Ryugu recorded by pyrrhotite

Dennis Harries, Toru Matsumoto, Falko Langenhorst, Takaaki Noguchi, Akira
Miyake, Yohei Igami, Mitsutaka Haruta, Yusuke Seto, Masaaki Miyahara,
Naotaka Tomioka, et al.

Incipient space weathering on asteroid 162173 Ryugu recorded by pyrrhotite

Dennis HARRIES [1,2,*], Toru MATSUMOTO[3,4], Falko LANGENHORST[1], Takaaki NOGUCHI[4],
Akira MIYAKE[4], Yohei IGAMI[4], Mitsutaka HARUTA[5], Yusuke SETO[6], Masaaki MIYAHARA[7],
Naotaka TOMIOKA[8], Hikaru SAITO[9,10], Satoshi HATA[11,12], Aki TAKIGAWA[13],
Yusuke NAKAUCHI[14], Shogo TACHIBANA[15], Tomoki NAKAMURA[16],
Megumi MATSUMOTO[16], Hope A. ISHII[17], John P. BRADLEY[17], Kenta OHTAKI[17],
Elena DOBRICĂ[17], Hugues LEROUX[18], Corentin LE GUILLOU[18], Damien JACOB[18],
Francisco de la PEÑA[18], Sylvain LAFORET[18], Bahae-eddine MOULOUD[18], Maya MARINOVA[19],
Pierre BECK[20], Van T. H. PHAN[20], Rolando REBOIS[20], Neyda M. ABREU[21], Jennifer GRAY[22],
Thomas ZEGA[23], Pierre-M. ZANETTA[23], Michelle S. THOMPSON[24], Rhonda STROUD[25],
Kate BURGESS[25], Brittany A. CYMES[26], John C. BRIDGES[27], Leon HICKS[27],
Martin R. LEE[28], Luke DALY[28,29,30], Phil A. BLAND[31], Michael E. ZOLENSKY[32],
David R. FRANK[17], James MARTINEZ[33], Akira TSUCHIYAMA[34,35,36], Masahiro YASUTAKE[37],
Junya MATSUNO[35], Shota OKUMURA[4], Itaru MITSUKAWA[4], Kentaro UESUGI[37],
Masayuki UESUGI[37], Akihisa TAKEUCHI[37], Mingqi SUN[35,36,38], Satomi ENJU[39],
Tatsuhiro MICHIKAMI[40], Hisayoshi YURIMOTO[41], Ryuji OKAZAKI[42], Hikaru YABUTA[7],
Hiroshi NARAOKA[42], Kanako SAKAMOTO[14], Toru YADA[14], Masahiro NISHIMURA[14],
Aiko NAKATO[43], Akiko MIYAZAKI[14], Kasumi YOGATA[14], Masanao ABE[14,44],
Tatsuaki OKADA[14,44], Tomohiro USUI[14,44], Makoto YOSHIKAWA[14,44], Takanao SAIKI[14,44],
Satoshi TANAKA[14,44], Fuyuto TERUI[45], Satoru NAKAZAWA[14,44], Sei-ichiro WATANABE[46], and
Yuichi TSUDA[14,44]

[1]Institute of Geoscience, Friedrich Schiller University Jena, Jena, Germany
[2]European Space Resources Innovation Centre, Luxembourg Institute of Science and Technology, Belvaux, Luxembourg
[3]The Hakubi Center for Advanced Research, Kyoto University, Kyoto, Japan
[4]Division of Earth and Planetary Sciences, Kyoto University, Kyoto, Japan
[5]Institute for Chemical Research, Kyoto University, Kyoto, Japan
[6]Department of Geosciences, Osaka Metropolitan University, Osaka, Japan
[7]Earth and Planetary Systems Science Program, Hiroshima University, Hiroshima, Japan
[8]Kochi Institute for Core Sample Research, X-Star, JAMSTEC, Nankoku, Japan
[9]Institute for Materials Chemistry and Engineering, Kyushu University, Fukuoka, Japan
[10]Pan-Omics Data-Driven Research Innovation Center, Kyushu University, Fukuoka, Japan
[11]Department of Advanced Materials Science, Kyushu University, Fukuoka, Japan
[12]The Ultramicroscopy Research Center, Kyushu University, Fukuoka, Japan
[13]Department of Earth and Planetary Science, University of Tokyo, Tokyo, Japan
[14]Institute of Space and Astronautical Science, Japan Aerospace Exploration Agency, Sagamihara, Japan
[15]UTokyo Organization for Planetary and Space Science, University of Tokyo, Tokyo, Japan
[16]Department of Earth Science, Graduate School of Science, Tohoku University, Sendai, Japan
[17]Hawai'i Institute of Geophysics and Planetology, the University of Hawai'i at Mānoa, Honolulu, Hawaii, USA
[18]Université de Lille, CNRS, INRAE, Centrale Lille, UMR 8207-UMET-Unité Matériaux et Transformations, Lille, France
[19]Université de Lille, CNRS, INRAE, Centrale Lille, Université Artois, FR 2638-IMEC-Institut Michel-Eugène Chevreul, Lille, France
[20]Institut de Planétologie et d'Astrophysique de Grenoble (IPAG), Université Grenoble Alpes, Grenoble, France
[21]Langley Research Center, NASA, Hampton, Virginia, USA
[22]Materials Characterization Lab, The Pennsylvania State University, Millennium Science Complex, University Park, Pennsylvania, USA
[23]Lunar and Planetary Laboratory, Department of Planetary Sciences, University of Arizona, Tucson, Arizona, USA
[24]Department of Earth, Atmospheric and Planetary Sciences, Purdue University, West Lafayette, Indiana, USA

[25]Materials Science and Technology Division, U.S. Naval Research Laboratory, Washington, DC, USA
[26]U.S. Naval Research Laboratory, Washington, DC, USA
[27]Space Research Centre, University of Leicester, Leicester, UK
[28]School of Geographical and Earth Sciences, University of Glasgow, Glasgow, UK
[29]Australian Centre for Microscopy and Microanalysis, University of Sydney, Sydney, New South Wales, Australia
[30]Department of Materials, University of Oxford, Oxford, UK
[31]School of Earth and Planetary Sciences, Curtin University, Perth, Western Australia, Australia
[32]ARES, NASA, Johnson Space Center, Houston, Texas, USA
[33]Jacobs Engineering, Dallas, Texas, USA
[34]Research Organization of Science and Technology, Ritsumeikan University, Kusatsu, Shiga, Japan
[35]CAS Key Laboratory of Mineralogy and Metallogeny/Guangdong Provincial Key Laboratory of Mineral Physics and Materials, Guangzhou Institute of Geochemistry, Chinese Academy of Sciences (CAS), Guangzhou, China
[36]CAS Center for Excellence in Deep Earth Science, Guangzhou, China
[37]Japan Synchrotron Radiation Research Institute, Sayo-gun, Hyogo, Japan
[38]University of Chinese Academy of Sciences, Beijing, China
[39]Department of Mathematics, Physics, and Earth Science, Ehime University, Matsuyama, Ehime, Japan
[40]Faculty of Engineering, Kindai University, Higashi-osaka, Japan
[41]Department of Earth and Planetary Sciences, Hokkaido University, Sapporo, Japan
[42]Department of Earth and Planetary Sciences, Kyushu University, Fukuoka, Japan
[43]National Institute of Polar Research, Tachikawa, Japan
[44]The Graduate University for Advanced Studies, Sokendai, Hayama, Japan
[45]Department of Mechanical Engineering, Kanagawa Institute of Technology, Atsugi, Japan
[46]Department of Earth and Environmental Sciences, Nagoya University, Nagoya, Japan

*Correspondence
Dennis Harries, Institute of Geoscience, Friedrich Schiller University Jena, Carl-Zeiss-Promenade 10, D-07745 Jena, Germany.
Email: dennis.harries@esric.lu

Abstract–Regolith samples returned from asteroid 162173 Ryugu by the Hayabusa2 mission provide direct means to study how space weathering operates on the surfaces of hydrous asteroids. The mechanisms of space weathering, its effects on mineral surfaces, and the characteristic time scales on which alteration occurs are central to understanding the spectroscopic properties and the taxonomy of asteroids in the solar system. Here, we investigate the behavior of the iron monosulfides mineral pyrrhotite ($Fe_{1-x}S$) at the earliest stages of space weathering. Using electron microscopy methods, we identified a partially exposed pyrrhotite crystal that morphologically shows evidence for mass loss due to exposure to solar wind ion irradiation. We find that crystallographic changes to the pyrrhotite can be related to sulfur loss from its space-exposed surface and the diffusive redistribution of resulting excess iron into the interior of the crystal. Diffusion profiles allow us to estimate an order of magnitude of the exposure time of a few thousand years consistent with previous estimates of space exposure. During this interval, the adjacent phyllosilicates did not acquire discernable damage, suggesting that they are less susceptible to alteration by ion irradiation than pyrrhotite.

INTRODUCTION

Asteroid Surface Evolution

Near-Earth asteroids (NEAs) are of special interest due to their record of the solar system's early evolution, their terrestrial impact hazard, and their potential role in future space resources utilization. Obtaining knowledge of these bodies mostly relies on remote characterization of their surfaces through telescopic or spacecraft observations. Our understanding of the present-day asteroid population and its history therefore largely depends on understanding the processes and their rates taking place in the uppermost layers of their regoliths.

The orbital parameters of NEAs vary on time scales of <0.01 Ma during their stay in the inner solar system (e.g., Michel & Delbo, 2010; Michel et al., 1996; Michel & Yoshikawa, 2005), and the dynamical lifetimes of NEAs

are on the order of 1–10 Ma (e.g., Gladman et al., 1997; Granvik et al., 2018). Hence, many NEAs may undergo surface modifications by tidal forces during repeated close encounters with planets.

Non-gravitational forces such as the Yarkovsky and YORP effects (Öpik, 1951; Rubincam, 2000) are expected to gradually alter orbital elements and change rotation rates and axial tilts through time. The YORP effect can induce increasing rotation rates of asteroids and potentially reshape surfaces and lead to disruption (e.g., Jewitt et al., 2010; Kaasalainen et al., 2007; Lowry et al., 2007; Taylor et al., 2007). The effects of comminution by thermal fatigue and impact gardening lead to additional changes to the surface regolith (e.g., Delbo et al., 2014; Housen et al., 1979).

Superposed on these mechanical changes to asteroid surfaces are the mineralogical effects of space weathering caused by the energetic ions of the solar wind, micro-meteoroid impacts, and other forms of physicochemical alteration, such as devolatilization through thermal activation. These processes are taking place at mineral surfaces directly exposed to the environment of space and progressively change the spectroscopic characteristics of the regolith (e.g., Pieters et al., 2000; Pieters & Noble, 2016).

The apparent time scale of changes to an asteroid's surface is a complex interplay of mechanical and physicochemical processes as outlined above. Understanding how regolith surfaces evolve through time is therefore an important step toward understanding the dynamical behavior of asteroids in the inner solar system and a proper taxonomical and compositional analysis of the present-day asteroid population. The mechanistic understanding of space weathering processes ultimately requires the return of samples and their microscopic study in terrestrial laboratories. JAXA's Hayabusa and Hayabusa2 spacecrafts have returned feature-rich inventories of space-weathered regolith from the asteroids 25143 Itokawa and 162173 Ryugu, respectively (Noguchi et al., 2011, 2023).

The samples of C-type asteroid Ryugu returned by Hayabusa2 have been linked to hydrous CI chondrites based on multiple mineralogical and isotopic constraints (Greenwood et al., 2023; Nakamura et al., 2022; Yada et al., 2022; Yokoyama et al., 2022). Space weathering on Ryugu has been found to produce hydroxyl-poor surface layers on phyllosilicate-bearing regolith particles through a complex combination of ion irradiation and deposition of impact-derived amorphous material (Noguchi et al., 2023). However, the time scales of the earliest onset of space weathering to full development and spectral cloaking of the hydroxyl absorption characteristics are not well constrained. Cosmogenic noble gases in Ryugu samples reveal exposure ages of ~5 Ma, corresponding to the residence time of a decimeter-thick surface regolith

and the injection of Ryugu into near-Earth space (Okazaki et al., 2022). The direct exposure of mineral surfaces to space is expected to be considerably shorter, on the scale of hundreds to thousands of years based on implanted solar wind gases and solar flare tracks (Noguchi et al., 2023; Okazaki et al., 2022). The structural and chemical responses of mineral surfaces can provide rough but complementary estimates of exposure times and constrain the mechanisms and consequences of space weathering. Here, we investigate the non-stoichiometric sulfide mineral pyrrhotite for its response to space exposure. Pyrrhotite is a characteristic minor mineral component of CM, CR, and CI chondrites typically occurring at <10 vol% modal abundances (Berger et al., 2016; Bullock et al., 2005; Harries & Langenhorst, 2013; Schrader et al., 2021; Singerling & Brearley, 2018). It occurs in abundances of 2–5 vol% in samples returned by Hayabusa2 (Nakamura et al., 2022; Okazaki et al., 2022). The loss of sulfur appears to be a characteristic devolatilization effect related to space weathering and has been detected remotely (Foley et al., 2006; Kracher & Sears, 2005; Nittler et al., 2001), experimentally (Christoph et al., 2022), and in returned samples from Itokawa and the Moon (Chaves & Thompson, 2022; Matsumoto et al., 2020, 2021). Pyrrhotite's structural diversity and chemical variability offer potential insight into this process.

Pyrrhotite Mineralogy

Pyrrhotites ($Fe_{1-x}S$) are nonstoichiometric iron monosulfides crystallizing in the NiAs structure type of hexagonally close-packed S atoms with octahedrally coordinated Fe atoms in interstitial layers perpendicular to the NiAs-based crystallographic c axis (e.g., Morimoto et al., 1975). Iron deficiency arises from Fe-site vacancies, which order into complex crystallographic superstructures. Most prevalent in nature are NC-type superstructures of which 4C-pyrrhotite (Fe_7S_8, $x = 0.125$) can be considered an endmember. Here, fully Fe-occupied octahedral layers regularly alternate with four symmetrically distinct vacancy-bearing layers, resulting in a monoclinic superstructure (e.g., Bertaut, 1953; Powell et al., 2004). Troilite (FeS) can be considered the other stoichiometric endmember, containing no Fe-site vacancies. Its superstructure, occasionally referred to as 2C-pyrrhotite but unrelated to NC-type structures, arises from structural distortion with respect to the NiAs aristotype and not from vacancy ordering (e.g., Skála et al., 2006).

Intermediate and non-integral NC-pyrrhotites, with N values typically ranging between 4 and 6, display highly variable superstructures coupled to Fe deficiency ($0 < x < 0.125$) and complex structural organization of Fe-site vacancies (e.g., Morimoto et al., 1975; Nakazawa & Morimoto, 1971). These structures have been described

in a four-dimensional superspace model (Izaola et al., 2007) and identified as commensurately and incommensurately modulated defect structures (Harries et al., 2011; Jin et al., 2021; Yamamoto & Nakazawa, 1982). The translation interface modulation model presented by Harries et al. (2011) and the superspace model of Izaola et al. (2007) couple the Fe deficiency x of bulk NC-pyrrhotite to the N value obtained from diffraction patterns via the relation $1/N = 2x$. Hence, it is possible to detect and quantify small variations in the Fe/S ratio from carefully collected diffraction patterns at small scale using transmission electron microscopy (TEM) and selected area electron diffraction (SAED).

Compared to TEM-based energy-dispersive X-ray spectroscopy (EDS) analysis of Fe/S ratios, the TEM-SAED approach allows a higher accuracy at comparable spatial resolution. TEM-EDS analysis suffers from several sources of systematic errors, including errors in sample thickness determination (for X-ray absorption correction), spurious Fe Kα spectral contributions from the TEM (by scattered electrons interacting with the pole pieces), and radiolytic effects on the sample (sulfur loss and accumulation of carbonaceous material during prolonged spot irradiation). The required accuracy and precision to determine Fe/S ratio in the narrow range of 0.875 (4C-pyrhotite) to 0.917 (6C-pyrrhotite) have thus far never been achieved using TEM-EDS. Wavelength-dispersive electron probe microanalysis (WDS-EPMA) on polished pyrrhotite samples with appropriate calibration and matrix correction has shown good agreement between Fe/S ratios measured and N values derived by TEM-SAED (Harries et al., 2011, 2013). However, the minimum analytical spot size of 2–3 μm in WDS-EPMA is not suitable for detailed analysis of the typically <10 μm-sized pyrrhotite crystals found in the Hayabusa2 samples. Hence, we used the TEM-SAED technique to study the effect of space exposure on pyrrhotite and the loss of sulfur from the mineral.

SAMPLES

The Hayabusa2 mission returned about 5.4 g of Ryugu's regolith from two distinct touch-down sites, TD1 and TD2, corresponding to chambers A (3.24 g) and C (2.03 g) of the sample collector, respectively (Tachibana et al., 2022; Yada et al., 2022). TD1 is located at the equatorial bulge region of the asteroid, and the samples from it are expected to represent typical space-exposed surface material. TD2 has sampled ejecta material from the Small Carry-on Impactor (SCI; Arakawa et al., 2020), and the samples are expected to contain a large fraction of freshly broken and subsurface material. The size range of particles comprises individual fragments of mm-sized down to micrometer-sized dust.

We have studied batch sample A0104 consisting of submillimeter fines obtained at TD1 to determine the effects of space weathering on directly space-exposed regolith (Noguchi et al., 2023). This sample had a mass of approximately 0.3 mg and comprised about 100 particles all >0.1 mm in size. The particles were screened by scanning electron microscopy for morphologies indicative of or consistent with space weathering.

For in-depth studies of individual particles and mineral grains, we extracted site-targeted electron transparent sections using the focused ion beam (FIB) method. The specific particle of the batch sample discussed here is designated A0104-00700600. For this work, FIB section A0104-00700601 (internal designation AP007_g06T1) of a pyrrhotite crystal partially exposed on the particle's surface was studied in detail.

METHODS

SEM-FIB

The surface of the pyrrhotite-bearing particle was studied at Kyoto University using a JEOL JSM-7001F field-emission scanning electron microscope (FESEM) after mounting the particle onto a gold substrate using a small drop of epoxy adhesive. A Helios NanoLab G3 CX FIB system at Kyoto University was then used to extract an electron transparent section targeting the pyrrhotite crystal and adjacent matrix. For this purpose, a target area (approximately $2 \times 15 \, \mu m$) of each Ryugu grain was coated with an electron beam-deposited Pt layer (at 2 kV) followed by a ion beam-deposited Pt layer (at 30 kV Ga$^+$). A small lamella (approximately $2 \times 15 \times 15 \, \mu m$) containing the target area was extracted from each grain using a 30-kV Ga$^+$ ion beam. The small lamella was then attached to a post of a Cu FIB grid using redeposited Cu from sputtering small areas (approximately $1 \times 5 \times 1 \, \mu m$ each) of the post just beside the lamella by the Ga$^+$ beam. After the lamella was attached to the post, Pt was also deposited onto the joint to strengthen its attachment to the post. The lamella was thinned to ~200 nm thickness using sequentially lower beam currents of 400 nA, then 240 nA, and finally 0.083 nA. The settings were reduced to 16 kV and 0.130 nA until the lamellae became ~100 nm thick. The damaged layers on the surfaces of the lamella were removed using a 2 kV Ga$^+$ beam at 77 pA. The acceleration voltage of the electron beam was 2 kV in all the FIB processing stages.

TEM

The extracted FIB section was studied by (scanning) TEM and SAED using a Tecnai G2 FEG at the University of Jena. The TEM was operated at 200 keV

electron energy and equipped with an Oxford $80\,mm^2$ SDD EDS detector, a Gatan UltraScan 2 k CCD camera, and a Fischione HAADF detector. During electron irradiation, the sample was cooled to $108 \pm 2\,K$ using a Gatan double-tilt analytical cooling holder. The projected size of the SAED aperture on the specimen image plane was 180 nm in diameter. For the crystallographic survey of the pyrrhotite crystal sectioned in our sample, we obtained SAED patterns across the crystal and recorded the corresponding aperture position with respect to a Cartesian coordinate system in the plane of the FIB section.

Crystallographic Analysis

The objective of the crystallographic analysis was to obtain accurate Fe/S ratios across the sectioned pyrrhotite crystal at high spatial resolution. The analysis of pyrrhotite TEM-SAED patterns here follows the procedure described in Harries et al. (2011) using a four-dimensional *hklm* indexing scheme. Here, *m* indexes the superstructure satellite reflections as multiples of the reciprocal modulation vector *q* with respect to the base structure. The modulation vector *q* in relation to the reciprocal lattice repeat *c** allows us to calculate *N* via the relation $N = c^*/q$. The *N* values obtained from the SAED patterns were converted to atomic Fe/S ratios via the relation $Fe/S = 1 - 1/(2N)$, which has been derived from the relation $1/N = \gamma = 2x$ (Harries et al., 2011; Izaola et al., 2007). Using our method, the standard error of *N* is typically about 0.04, resulting in a standard uncertainty of about 0.0008 in the Fe/S ratio. Small Ni contents, on the order of 0.4 ± 0.1 at% as indicated by EDS analysis, are not resolved by the crystallographic analysis and are included in the Fe/S ratio as equivalent to Fe.

Diffusion Modeling

The Fe/S ratios obtained from SAED were interpolated across the pyrrhotite crystal using ordinary Kriging in the R package *gstat* (Pebesma, 2004). Interpolation was necessary to extract spatially representative chemical (Fe/S) profiles and to estimate variances of the composition from the discrete SAED patterns distributed across the crystal and near its margins. We chose an exponential model to fit the variogram obtained from the Cartesian coordinates of SAED patterns in the sample plane and the Fe/S ratios obtained from them. Other models tested were spherical, Gaussian, and wavelet functions producing similar results (Figure S1; Discussion section).

Theoretical profiles of the atomic Fe/S ratios as function of depth *x* and time *t* were modeled assuming semi-infinite diffusion of iron atoms from the top of the crystal having a 6C composition (Fe/S = 11/12 = 0.92)

into the bulk crystal having a 5C composition (Fe/S = 9/10 = 0.90):

$$\left(\frac{Fe}{S}\right)(x, t) = \left(\frac{Fe}{S}\right)_{surf} + \left[\left(\frac{Fe}{S}\right)_{bulk} - \left(\frac{Fe}{S}\right)_{surf}\right] erf\left(\frac{x}{2\sqrt{Dt}}\right)$$

Low-temperature diffusion coefficients *D* ($<589\,K$) were calculated based on experimental data by Herbert et al. (2015) to account for the control of iron self-diffusion by magnetic effects below the Néel temperature (the temperature of the antiferromagnetic to paramagnetic transition). The diffusion coefficient of iron in pyrrhotite also depends on the concentration of Fe-site vacancies and, therefore, on the Fe/S ratio, as well as on the crystallographic orientation of the diffusion direction (Condit et al., 1974). However, the effects of both factors lead to variations in the diffusion coefficient within about one order of magnitude (Herbert et al., 2015), which is small relative to the order-of-magnitude variations due to temperature. Hence, for the zeroth-order approximation in the present work, these effects have been neglected due to the large uncertainty in temperature to which the sample was naturally exposed (see below).

RESULTS

External Morphology of Pyrrhotite

SEM images of the regolith particle studied show a fine-grained phyllosilicate surface with two prominent, euhedral pyrrhotite crystals and μm to sub-μm-sized magnetite crystals forming poorly developed framboidal aggregates (Figure 1). The phyllosilicate surface is rough and does not show signs of smoothing as observed on more intensely space-weathered Ryugu samples (Noguchi et al., 2023). The pyrrhotite crystals show six-sided, tabular habits and reach sizes between 10 and 12 μm diameter. One of them is partially embedded in the phyllosilicate matrix and displays a pitted and rough surface morphology in places where it is not covered by phyllosilicates. Similar morphologies of space-exposed pyrrhotite crystals in Ryugu samples have been reported recently by Nakato et al. (2022, 2023) and Matsumoto et al. (2022).

The FIB cross section of the crystal (Figures 2a and 3) shows planar crystal faces where it is covered by phyllosilicates and irregular boundaries where it is not. The crystal morphology based on the SAED patterns comprises the dominant {001} basal forms, the {010} prisms, and the {011} pyramids (assuming hexagonal point-group symmetry). Extrapolating the straight crystal boundaries suggests that some volume of the exposed crystal surface
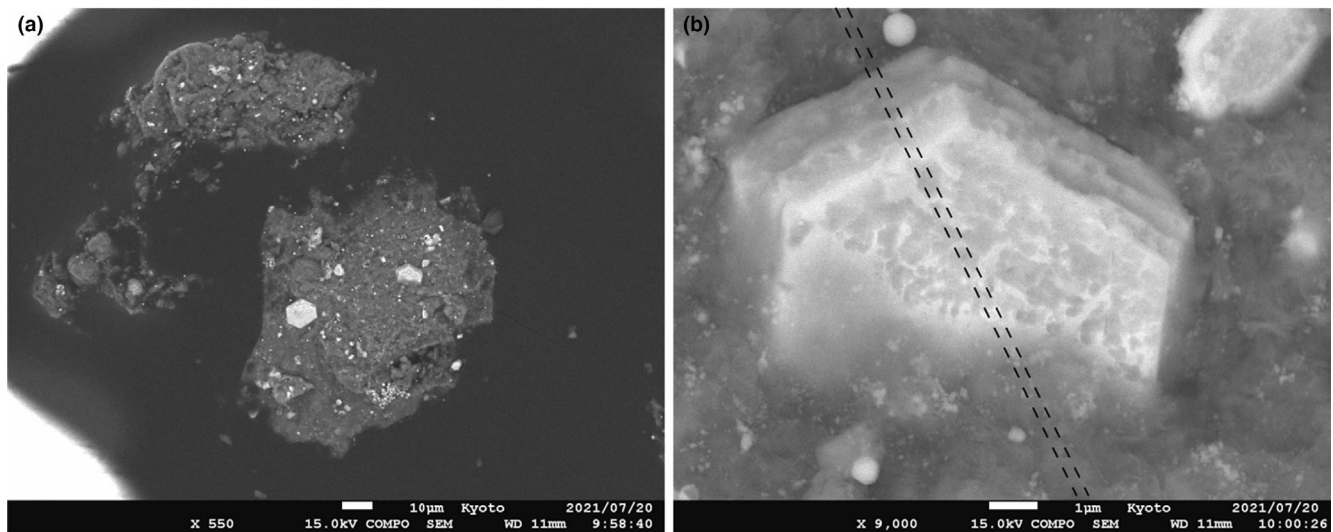
FIGURE 1. SEM-BSE images of the regolith particle A0104-00700600 studied. (a) Overview. (b) Detail of the pyrrhotite crystal sampled by FIB section A0104-00700601 (dashed lines). The euhedral crystal shows a rough surface where exposed from the surrounding phyllosilicate matrix.

has been lost (Figure 2a). Detailed EDS mapping of the interface between the exposed sulfide and the deposited platinum did not reveal the presence of vapor-deposited material containing Mg, Si, or O. Such material has been observed on sulfide and metal surfaces of samples returned from asteroid 25143 Itokawa and was interpreted to indicate prolonged space weathering that led to mobilization and re-depositioning of silicate material by micrometeoroid impacts (Matsumoto et al., 2020).

Mineral Association

The pyrrhotite crystal studied is embedded in fine-grained, interlocking phyllosilicate material that shows the basal 001 diffraction maximum of serpentine at approximately 0.71–0.73 nm. Their composition, determined by EDS, is indicative of a small scale, about equimolar mixture of serpentine and smectite/saponite, showing a molar $(Mg + Fe)/Si$ ratio of 0.93 ± 0.04. The phyllosilicates are Mg-rich with a molar $Mg/(Mg + Fe)$ of 0.93 ± 0.01, consistent with analyses of other samples of Ryugu (Noguchi et al., 2023). Molar Na/Si and Al/Si ratios of approximately 0.06 indicate small degrees of substitution of Mg and Si. Other phases present in the FIB section are nm-sized Fe- and Ni-rich sulfides (probably pentlandite) and macromolecular organic globules embedded in the phyllosilicates but not in direct contact with the sulfide.

Internal Defect Microstructures in Pyrrhotite

The pyrrhotite crystal studied contains a high number density of dislocations in multiple geometric configurations

pervading the entire crystal (Figure 2b–f). Linear, up to 1 μm long dislocations with dislocation lines parallel to [001] are most abundant and show a number density up to approximately $2 \times 10^{13}\,m^{-2}$. Dislocations aggregated into subgrain boundaries and isolated dislocation loops occur subordinately. The linear dislocations are apparently glissile with the combination 1/3[110](001) acting as a slip system. Subgrain boundaries and dislocation loops occur in the vicinity of internal voids that might have once been filled with fluid, as found in other Ryugu samples (Nakamura et al., 2022). Bright-field TEM images and SAED patterns also indicate the presence of multiple microtwins on the (001) plane throughout the entire grain (Figure 4).

Spatial Distribution of Crystallographic Structures and Fe/S Ratios in Pyrrhotite

The geometrical analysis of SAED patterns acquired in various places across the pyrrhotite crystal indicates that the interior is mostly characterized by nonintegral N values between 4.8 and 5.1, corresponding to intermediate Fe/S ratios (Figures 2 and 4). N values close to 4.0, indicating low-Fe/S 4C-pyrrhotite, are found in the part of the crystal most deeply embedded in the phyllosilicate matrix. SAED patterns obtained closer to the exposed surface show N values systematically larger than 5.1, gradually reaching up to 5.9 near the edge of the crystal. Some patterns at the edge do not display superstructure reflections, suggesting the nanoscale occurrence of troilite.

The overall distribution of N values shows a pronounced contrast between the exposed crystal surface
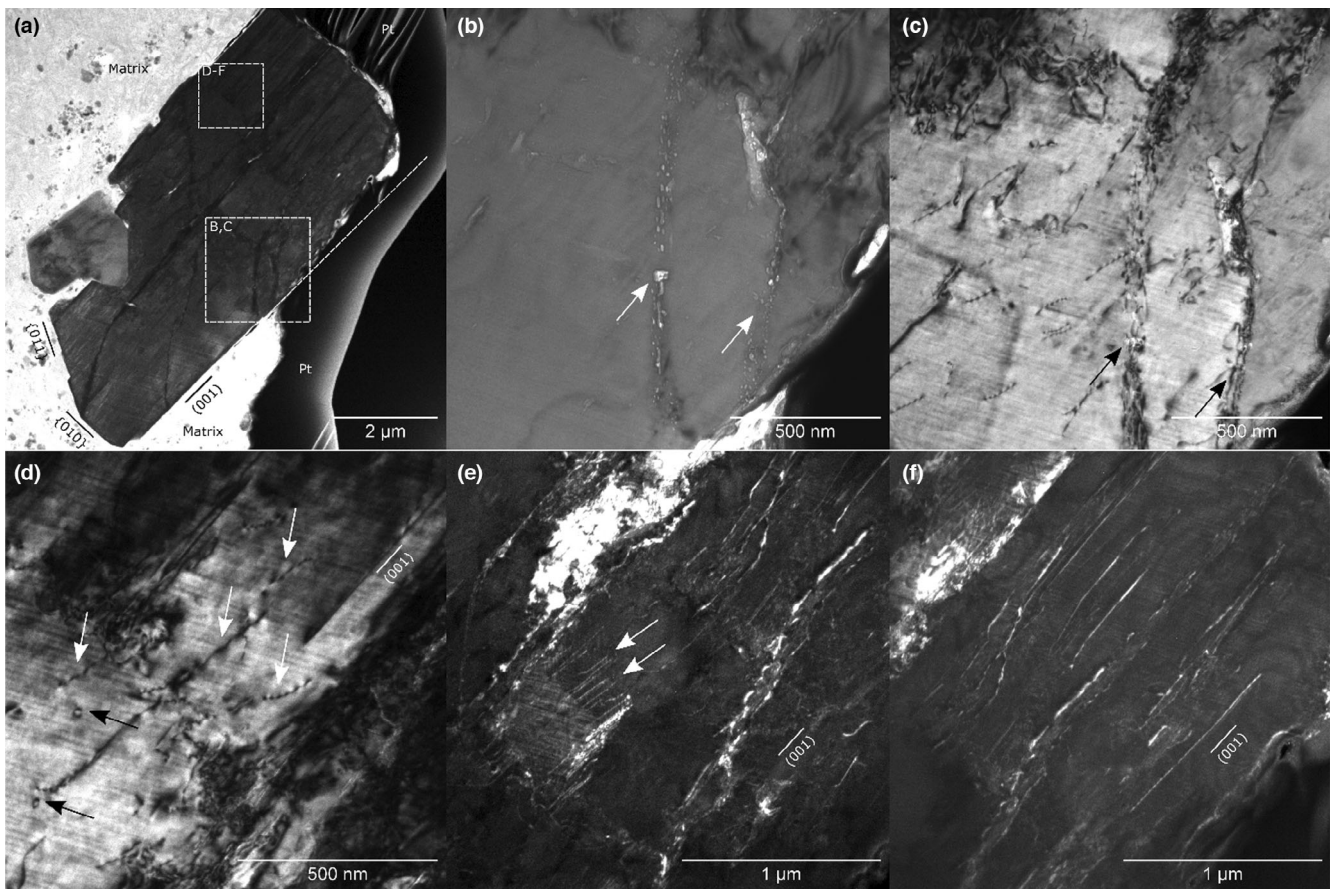
FIGURE 2. TEM micrographs of the pyrrhotite crystal (shown in Figure 1b) within the FIB section. (a) Overview image showing the euhedral crystal morphology in the buried parts and the possible mass loss on the exposed surface (dashed line). In the buried part, the crystal shows clean faces (marked with their respective indices). A subgrain on the left side shows a different diffraction contrast due to a large angular misalignment. (b) TEM bright-field images showing trails of voids (arrows), interpreted as fluid inclusions. (c) TEM dark-field image corresponding to (b). The trails of fluid inclusions are accompanied by dislocations, forming a low-angle subgrain boundary (arrows at positions corresponding to arrows in (b)). Striations at about 20° from the horizontal are thickness variations due to the FIB process. (d) TEM dark-field image showing helical dislocations (white arrows) and dislocation loops (black arrows). Striations at about 20° from the horizontal are thickness variations due to the FIB process. (e,f) TEM dark-field images showing straight, perfect dislocations in glide configuration. The slip system is 1/3 [110](001).

and the buried parts, indicating that the situation of being buried or exposed influenced the chemical composition of the crystal. Converting the N values to Fe/S ratios and interpolating across the crystal adds to this picture, showing that Fe/S increases from the most buried (atomic Fe/S $\approx 7/8$ of 4C-pyrrhotite) to the topmost exposed region (atomic Fe/S $\approx 11/12$ of 6C-pyrrhotite or Fe/S ≈ 1 of troilite).

Diffusive Redistribution of Iron

The extracted profiles of Fe/S ratios from the topmost exposed surface into the interior of the crystal show a non-linear gradient, indicating a redistribution of Fe site vacancies by bulk diffusion of iron atoms

(Figure 5). Modeling of the diffusion profiles assuming 6C-pyrrhotite at the surface, 5C-pyrrhotite in the interior, and a temperature range of 310–360 K, covering the maximum diurnal surface temperatures determined by Shimaki et al. (2020), yields the time–temperature relationship shown in Figure 6.

At the average maximum surface temperature of 339 K, the diffusion time scale required for the observed diffusion profiles is about 1.5 ka. Because the Arrhenian dependency of the diffusion coefficient on temperature is highly nonlinear, the peak daytime surface temperature is expected to have by far the most dominant effect on the diffusion profile. Our model is simplistic in neglecting the recession of the crystal surface by material loss and the finite dimension of the pyrrhotite crystal. However,
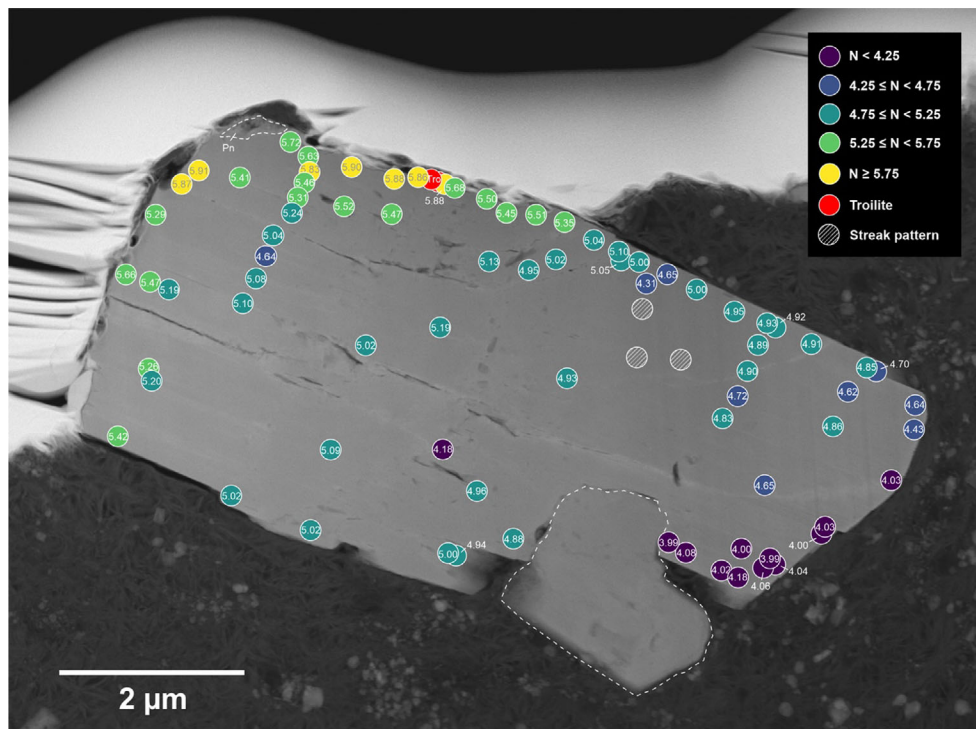
FIGURE 3. STEM-HAADF image of the pyrrhotite crystal (shown in Figure 1b) within the FIB section. Color-coded circles represent the locations of SAED patterns, with the corresponding superstructure N values obtained from these patterns. The region at the bottom, highlighted by the dashed line, is another pyrrhotite crystal with a large tilt of its crystallographic axes relative to the main crystal. No SAED patterns in useful zone axes could be obtained from this crystal. The region labeled Pn at the top of the crystal is Ni-rich and probably pentlandite.

we consider these sources of error as small relative to the uncertainty arising from the unknown effective temperature at which diffusion occurred.

At the equatorial latitude of the sampling site on Ryugu, the ±12 K standard deviation of the spatial average of the diurnal maximum temperature stated by Shimaki et al. (2020) covers nearly the whole range of temperature variation. This variation translates to a range of 0.3–8 ka in diffusion time if the extrema are taken as effective, constant temperatures. Limb temperatures of ≤230 K at dusk reported by Shimaki et al. (2020) correspond to diffusion time scales longer than the age of the solar system, such that nighttime on Ryugu essentially halts the diffusive redistribution of iron in surface-exposed pyrrhotite.

As night prevails for 50% of the time and shallow incidence of light on the day side reduces temperatures below the maximum for much of the time, the time–temperature relationship of Figure 6 provides lower duration limits for the diffusive redistribution, that is, the effective temperature of diffusion is always lower than the maximum surface temperature at a given location. The actual exposure time should be within a factor of roughly two to four (the latter because the cross-sectional

area of an assumed spherical shape of Ryugu is a quarter of its surface area).

The strong temperature dependency of diffusion and the nonuniform spatial and temporal distribution of temperatures on Ryugu is a source of uncertainty, and, therefore, hampers a straightforward interpretation of the rate of sulfur loss. Although the sampling site on the equatorial ridge likely reduces the influence of seasonal temperature variations, annual variations due to eccentricity and long-term orbital variations remain as additional sources of uncertainty. However, an exposure time of >1 ka and <10 ka appears to be a reasonable order-of-magnitude estimate of the time scale required for the distribution of iron observed in the pyrrhotite crystal studied.

DISCUSSION

Sulfur Loss during Space Weathering

The striking structural and chemical contrast between the pyrrhotite beneath the exposed surface and the pyrrhotite shielded by the matrix strongly suggests that space weathering played a major role in establishing this
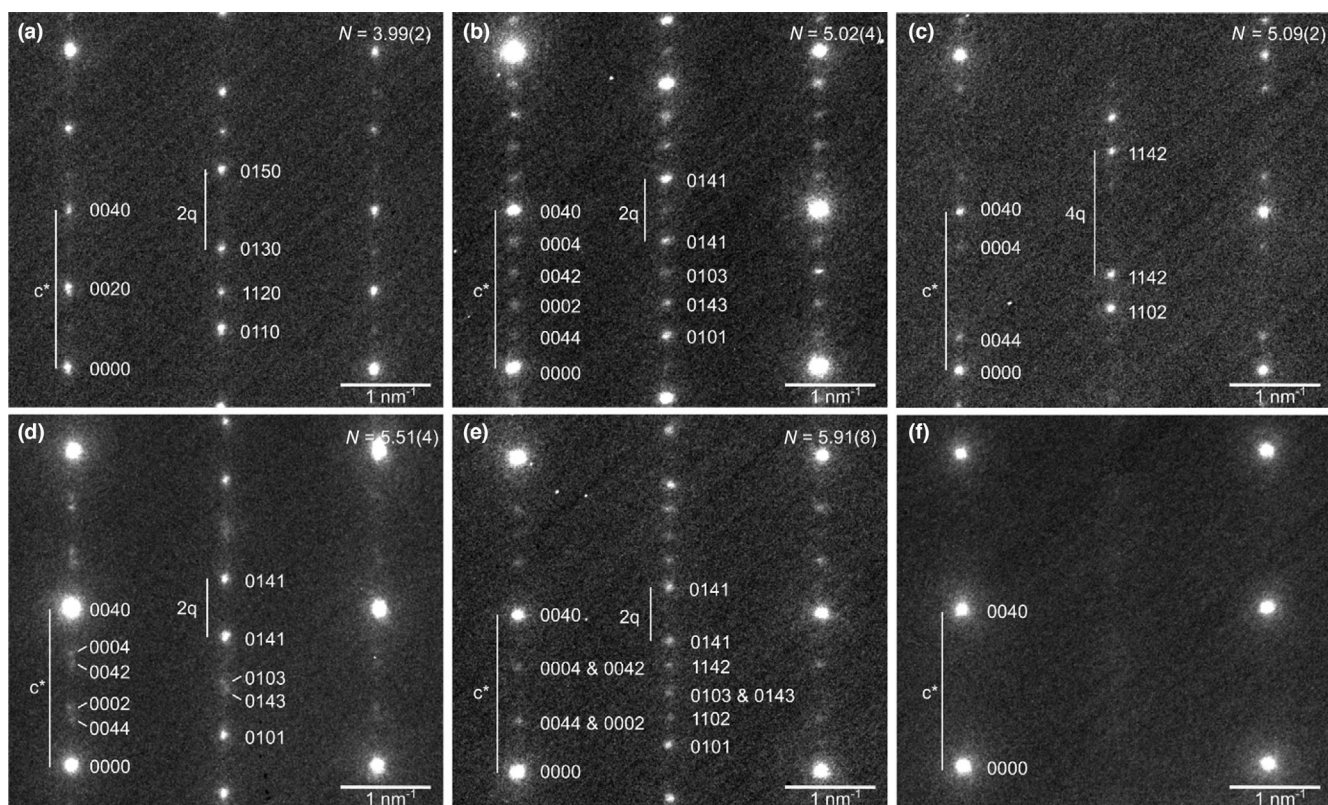
FIGURE 4. Selected TEM-SAED patterns from the pyrrhotite crystal shown in Figure 3. The patterns shown are sections of the full SAED patterns to highlight the relevant geometries. Indexing follows the 4H scheme outlined in Harries et al. (2011). The spot equivalent to the transmitted beam is marked 0000. (a) Pattern of twinned 4C-pyrrhotite. c^* marks the reciprocal repeat of the base structure's unit cell, q is the repeat of the superstructure. The crystal is strongly twinned indicated by the presence of $0\bar{1}lm$ and $1\bar{1}lm$ reflections in the central row, corresponding to zone axes [100] and [110]. This is common in 4C-pyrrhotite. (b–e) Patterns of NC-pyrrhotite with N of 5.02, 5.09, 5.51, and 5.91. (b), (c), and (d) are pure twin domains with either $0\bar{1}lm$ or $1\bar{1}lm$ reflections (zone axes [100] or [110], respectively). (e) is a mixed case with both twin domain present in the pattern representing zone axes [100] and [110]. (f) Pattern showing no superstructure reflections as expected for troilite in this zone axis geometry, being either [100] or [110].
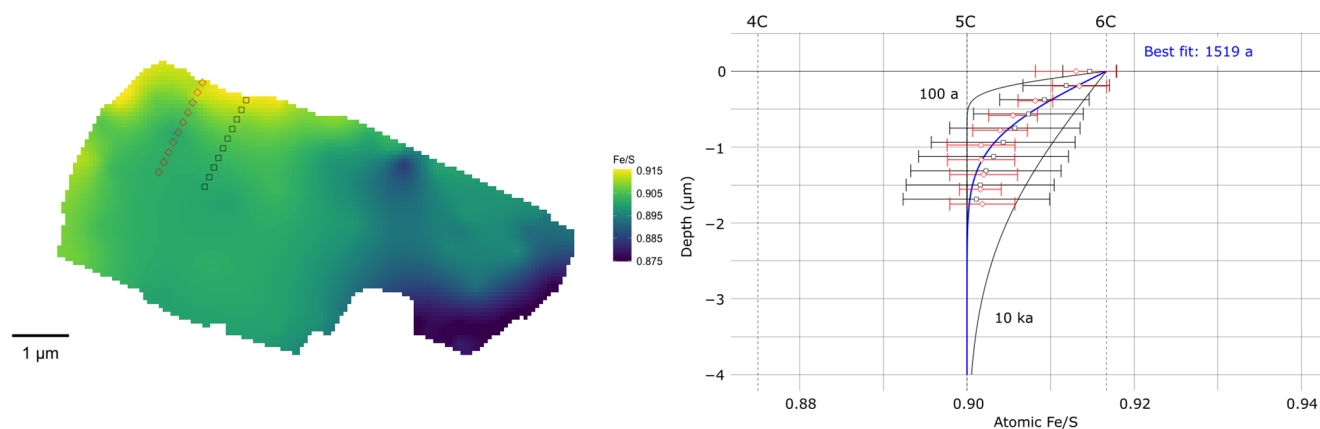

FIGURE 5. Interpolated atomic Fe/S ratios across the pyrrhotite crystal studied (Figure 3). Kriging interpolation used an exponential variogram model. Based on these continuous data, two profiles of Fe/S as a function of depth were extracted (diamond and square symbols). The best fit of a semi-infinite diffusion model to both profiles, assuming 6C-pyrrhotite at the surface, 5C-pyrrhotite in the bulk, yields a diffusion time of approx. 1.5 ka at a temperature of 339 K (see Figure 6). Error bars correspond to 2-sigma standard deviations and were obtained from the variance of the Kriging interpolation. Other variogram models yielded essentially indistinguishable results (cf. Figure S1).
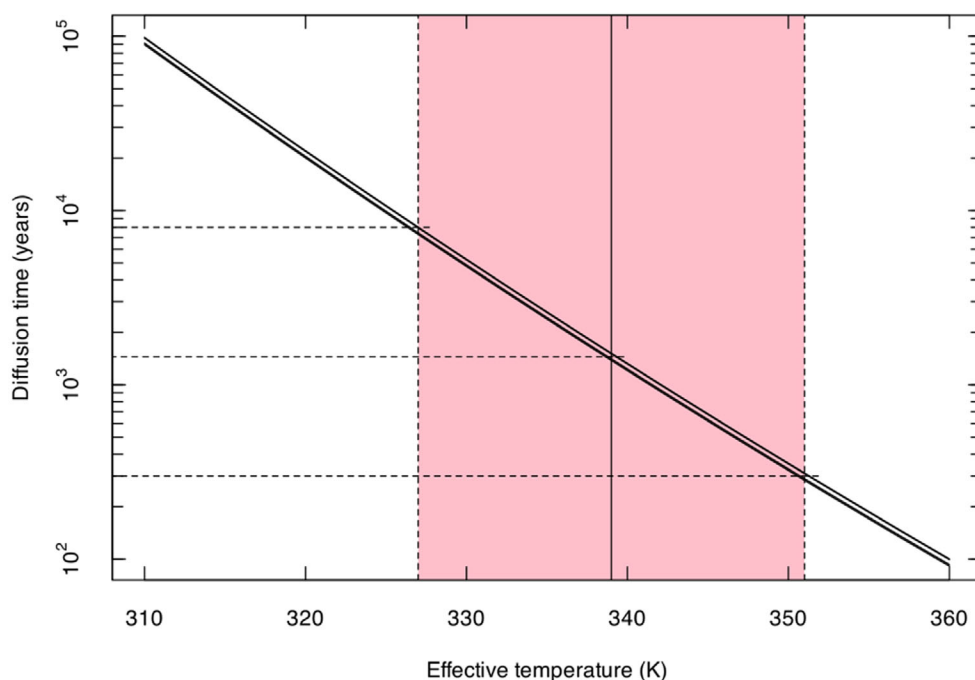
FIGURE 6. Diffusion time required to produce the diffusion profiles of Figure 5 as a function of effective diffusion temperature. Under non-isothermal conditions, the effective diffusion temperature corresponds to the time-averaged diffusion coefficient. This is unknown for Ryugu's surface at the location of the specimen studied here. Because the diffusion coefficient follows an Arrhenius relation with exponential dependence on temperature, the highest temperatures have the most profound effects on diffusion rates. Therefore, the maximum diurnal temperatures of Ryugu are shown (light red interval), centered on the average maximum of 339 ± 12 K (Shimaki et al., 2020). The multiple curves shown correspond to the different variogram models used for Kriging interpolation (Figure S1). At 339 K, the diffusion time corresponds to approx. 1.4–1.5 ka. At the lower limit of the interval given by Shimaki et al. (2020) of 327 K, the diffusion time required is about 8 ka. At the upper limit of 351 K, the time reduces to about 0.3 ka.

heterogeneous state. The multiple coexisting pyrrhotite variants across the crystal cannot be in thermodynamic equilibrium, as the phase rule allows at most two stable phases to coexist in the two-component (Fe, S) system.

On the micrometer scale, natural NC-pyrrhotites from terrestrial and extraterrestrial occurrences are often in exsolution relationships with 4C-pyrrhotite or troilite. Polysynthetic microtwinning and complex mesoscale structure along phase boundaries of exsolved pyrrhotites occur frequently as a result of crystal growth and low-temperature phase equilibration (e.g., Harries et al., 2011). Typical two-phase associations are 4C-pyrrhotite and NC-pyrrhotite with $N \approx 4.8$ to 4.9 as well as troilite and NC-pyrrhotite with $N \approx 5$ to 6 (Harries et al., 2011, 2013; Harries & Langenhorst, 2013; Jin et al., 2021; Morimoto et al., 1975). These pairs either are stable assemblages or are in the process of unmixing toward a stable assemblage. The latter metastable state might be frozen-in due to slow diffusion below 100°C as suggested by the observed (narrow) variability of the N values of coexisting pyrrhotite in terrestrial and meteoritic samples.

The bulk mineralogy of the pyrrhotite crystal studied here, consisting of frequently detected NC-pyrrhotite near

$N \approx 4.9$ and 4C-pyrrhotite in the buried part, is consistent with the observation of such phase assemblages in terrestrial pyrrhotites. CI chondrites typically contain 4C-pyrrhotite (e.g., Berger et al., 2016) and also the pyrrhotites within the samples of Ryugu have been identified by X-ray diffraction to be predominantly the 4C superstructure (Nakamura et al., 2022; preliminary TEM-SAED studies of small, buried pyrrhotite crystals in Ryugu samples confirm this). The coexistence with NC-pyrrhotite would not be unexpected based on the terrestrial observations, but the structural gradients and high diversity of different NC superstructures in our sample clearly indicate disequilibrium and point to the loss of sulfur from the surface.

It might be argued that disequilibrium may arise from rapid cooling. In this case, one would expect that NC pyrrhotites coexist with either troilite or 4C-pyrrhotite, albeit with N values that are far from the typical (near-)equilibrium values due to being frozen-in at elevated temperatures where the diffusion rate is outpaced by the cooling rate. However, the gradient of N values observed in our sample is not simply a frozen-in two-phase assemblage. It is a gradient across the crystal

between two endmembers—troilite near the surface, 4C-pyrrhotite at the most buried end—that based on heuristics should not coexist in (near-)equilibrated pyrrhotites. A temperature gradient across the crystal cannot explain this alone, as the 4C-pyrrhotite and troilite are separated by a chemical divide. Hence, an externally imposed chemical gradient must exist.

The mechanism of sulfur loss at the exposed surface of pyrrhotite may be the direct volatilization of S_2 into the vacuum of space, the selective sputtering of S by solar wind ions, the implantation of hydrogen derived from the solar wind, forming H_2S (Matsumoto et al., 2020), or a combination of these processes.

Regarding thermodynamically controlled thermal outgassing, pyrrhotite can be understood as a binary solid solution between stoichiometric FeS and a hypothetical endmember $\square$S consisting only of a hexagonal close-packed sulfur lattice and Fe-site vacancies (denoted by the $\square$ square symbol; Waldner & Pelton, 2005). At any given activity of $\square$S in the solid solution, a corresponding fugacity of S_2 in the adjacent gas phase arises via the equilibrium $\square S \rightleftharpoons \frac{1}{2}S_2$. Using the S_2 fugacity relations of Toulmin and Barton (1964) and Rau (1976), the loss of sulfur from stoichiometric troilite on the surface of asteroid Itokawa has been found to be extremely small by this process, due to the extremely small vapor pressure of S_2 over stoichiometric FeS (Matsumoto et al., 2020; $pS_2 \sim 10^{-36}$ Pa re-calculated at 339 K). Accordingly, the observed loss of sulfur and formation of metallic iron whiskers was attributed to the implantation of solar wind hydrogen and the formation of H_2S.

In the case of Fe-deficient 4C-pyrrhotite, the equilibrium pressure of S_2 is orders of magnitude larger, amounting to $pS_2 \sim 10^{-16}$ Pa at 339 K. Hence, the initial evaporation rate of S into the vacuum of space would also be orders of magnitude larger, amounting to $\sim 6 \times 10^9$ atoms/cm^2/year as calculated through the Hertz–Knudsen–Langmuir relationship (i.e., a linear kinetic rate law; Matsumoto et al., 2020; Tachibana & Tsuchiyama, 1998; Tsuchiyama et al., 1997) assuming an evaporation coefficient of $\alpha = 1$. This rate corresponds to a recession rate of the pyrrhotite surface of $\sim 2 \times 10^{-6}$ nm/year, which is a maximum value as the evaporation coefficient is expected to be significantly smaller than unity based on experimental study of stoichiometric FeS (Tachibana & Tsuchiyama, 1998).

While the above recession rate is about 12 orders of magnitude faster than for troilite on the surface of Itokawa, the mass loss through direct evaporation into space is insignificant relative to the observed surface roughness and apparent recession of the exposed pyrrhotite surface relative to the shielded crystal. Without the simplifications applied above, the rate of recession would be even lower due to lower temperature (i.e., below

the 339 K average diurnal maximum), and evaporation coefficient below unity, and the gradual build-up of excess Fe/S at the exposed surface, which would compositionally evolve toward stoichiometric FeS. The latter process would reduce pS_2 and the corresponding evaporation rate. At this stage, the sulfur loss would be controlled by the diffusive redistribution of excess iron into the interior of the crystal according to the reaction $FeS \rightleftharpoons \frac{1}{2}S_2 + Fe^{2+} + 2e^-$. As in the case of Itokawa troilite, it becomes clear that direct evaporation of S_2 into space alone cannot account for the observed corrosion and recession of the exposed pyrrhotite.

The selective sputtering of sulfur by solar wind ions has been studied experimentally as a possible mechanism for explaining the S depletion of S-type asteroid Eros (Loeffler et al., 2008). It was found that the combination of sputtering and laser-simulated meteoroid impacts can increase the Fe/S ratio significantly due to the selective removal of sulfur. The direct effect of ion irradiation alone was found to cause less S depletion on laboratory time scales, as diffusion from the bulk of the irradiated troilite was slow and the maximum penetration depth of the simulated solar wind He$^+$ ions is only on the order of 100 nm. Longer diffusion time scales, elevated temperatures, and higher diffusivity in pyrrhotite relative to troilite might lead to surface depletion of sulfur and the diffusive redistribution of iron as observed in our sample. However, the experiments were conducted with chemically inert helium, which in the natural solar wind composition is complementary to about 95% of hydrogen, which is chemically reactive.

Following the reasoning of Matsumoto et al. (2020), we hypothesize that the action of implanted hydrogen, acting to volatilize sulfur as H_2S, accelerates the loss of sulfur from the sulfide surface. This process proceeds through the reaction $FeS + 2H \rightleftharpoons H_2S + Fe^{2+} + 2e^-$. Unlike the case of Itokawa troilite, no formation of metallic iron whiskers has taken place in the sample studied here, because the Fe/S ratio has barely reached unity, which prevented the nucleation and growth of metallic iron (e.g., Tsuchiyama et al., 1997).

Vesicles at the surface of the pyrrhotite have not formed as in the case of Itokawa troilite. The reason for this might be the much higher diffusive mobility of iron (or Fe^{2+} and its associated electrons) in the vacancy-bearing bulk pyrrhotite, which leads to rapid redistribution of iron rather than the formation of complex surface structures. The detection of iron whiskers on highly modified pyrrhotite surfaces of Ryugu samples by Matsumoto et al. (2022) indicates that the pyrrhotite here represents the early stages of sulfur loss, which will progress similar to Itokawa troilite once the sulfide is saturated by iron (Fe/S = 1) and sulfur loss through solar wind irradiation continues.

Time Scale of Sulfur Loss

The sulfur loss observed in the pyrrhotite sample studied here occurred over a time period of 1–10 ka as suggested by the diffusion profile observed. This is consistent with the estimated rate of sulfur loss on asteroid Itokawa (Matsumoto et al., 2020), where severe sulfur depletion and growth of metallic iron whiskers occurred on a time scale of approximately 1–8 ka based on the number density of solar flare tracks in olivine. The exposure time of small, submillimeter-sized regolith particles on the surface of Ryugu appears to be similar, indicated by the density of solar flare tracks in a rare olivine crystal that corresponds to approximately 6 ka exposure (Noguchi et al., 2023). In that case, the adjacent phyllosilicate developed a noticeable surface alteration of about 20 nm thickness due to solar wind irradiation. Such alteration features leading to smoothing of the surface (Noguchi et al., 2023) are not observed in our sample, suggesting that the exposure was rather in the lower end of the interval of 1–10 ka estimated from the diffusion profiles.

Differential Susceptibility to Space Weathering

The observed alteration effects in pyrrhotite are from the early stages of space weathering on Ryugu, as neither the formation of metallic iron on the sulfide surface has taken place nor was any discernable alteration of the phyllosilicate surface detected. At this incipient stage, it is a notable observation that the phyllosilicates appear to be less susceptible to solar wind damage than the sulfide surface.

Progressive space weathering beyond the degree observed here is expected to weaken the hydroxyl absorption band of phyllosilicates at 2.7 μm (Noguchi et al., 2023). Following our observations, we suggest that this effect becomes apparent only after a few thousand years of direct space exposure. This is consistent with the onset of phyllosilicate alteration at time scales >3 ka determined by Noguchi et al. (2023) based on sample observations and irradiation experiments.

Christoffersen and Keller (2011) have shown that FeS is resistant to amorphization under high-energy Kr^{2+} ion irradiation, much in contrast to anhydrous silicates. The higher susceptibility of Fe sulfides to undergo space weathering via the irradiation by low-energy solar wind ions is possibly related to the highly volatile nature of sulfur, easily forming gaseous species such as H_2S, H_2S_2 (Zhu et al., 2019), and potentially HS radicals and elemental S species. This process is aided by the high diffusive mobility of iron in the monosulfides, especially if high number densities of vacancies are present, such as in pyrrhotite.

Shock Deformation

The defect microstructures observed, such as polysynthetic twinning, dislocation loops, internal voids, and subgrain boundaries, are likely defects produced during the growth of the crystal and subsequent re-ordering of the iron-site vacancies. The activation of a large number of perfect dislocations is an expected response of monosulfides to low shock loading. We did not observe extensive formation of partial dislocations and stacking faults as observed in highly shocked monosulfides (Langenhorst et al., 2014; Mang et al., 2012). Also, the absence of impact-derived vapor deposits of Si- and Mg-rich material on the exposed crystal suggests that hot impact ejecta or vapors did not contribute to the modification of the pyrrhotite surface. Such deposits were observed on samples of asteroid 25143 Itokawa that showed more intense space weathering features, including sulfur loss, than observed here (Matsumoto et al., 2020).

Although no direct evidence of impact is observed on the sample's surface, we interpret the pervasive dislocations present as indicative of weak shock loading affecting the entire grain. This is in contrast to local shock effects expected in micrometer-sized or submicrometer-sized impact events. Possibly, the event responsible for the pervasive dislocations could have been associated with the breaking of the original rock and the exposure of the pyrrhotite crystal. The absence of micro-cratering and the pervasive nature of the dislocations observed suggest that this might have occurred in a collision cascade within the regolith, explaining the low degree of shock deformation.

CONCLUSIONS

Our study of Ryugu particle A0104-00700600 indicates that pyrrhotite exposed to space at the heliocentric distances of the near-Earth environment loses sulfur on time scales of a few thousand years. This sulfur loss and the related structural and morphological changes are likely among the first effects of incipient space weathering before changes to the exposed phyllosilicate surfaces become apparent. The higher susceptibility of pyrrhotite to solar wind-induced alteration provides the potential to study the earliest stages of space weathering if spectral differences between Fe-deficient pyrrhotite and stoichiometric troilite could be leveraged.

REFERENCES

Arakawa, M., Saiki, T., Wada, K., Ogawa, K., Kadono, T., Shirai, K., Sawada, H., et al. 2020. An Artificial Impact on the Asteroid (162173) Ryugu Formed a Crater in the Gravity-Dominated Regime. *Science* 368: 67–71.

Berger, E. L., Lauretta, D. S., Zega, T. J., and Keller, L. P. 2016. Heterogeneous Histories of Ni-Bearing Pyrrhotite and Pentlandite Grains in the CI Chondrites Orgueil and Alais. *Meteoritics & Planetary Science* 51: 1813–29.

Bertaut, E. F. 1953. Contribution a l'etude des structures lacunaires: la pyrrhotine. *Acta Crystallographica* 6: 557–561.

Bullock, E. S., Gounelle, M., Lauretta, D. S., Grady, M. M., and Russell, S. S. 2005. Mineralogy and Texture of Fe-Ni Sulfides in CI1 Chondrites: Clues to the Extent of Aqueous Alteration on the CI1 Parent Body. *Geochimica et Cosmochimica Acta* 69: 2687–2700.

Chaves, L. C., and Thompson, M. S. 2022. Space Weathering Signatures in Sulfide and Silicate Minerals from Asteroid Itokawa. *Earth, Planets and Space* 74: 124.

Christoffersen, R., and Keller, L. P. 2011. Space Radiation Processing of Sulfides and Silicates in Primitive Solar Systems Materials: Comparative Insights from In Situ TEM Ion Irradiation Experiments. *Meteoritics and Planetary Science* 46: 950–969.

Christoph, J. M., Minesinger, G. M., Bu, C., Dukes, C. A., and Elkins-Tanton, L. T. 2022. Space Weathering Effects in Troilite by Simulated Solar-Wind Hydrogen and Helium Ion Irradiation. *Journal of Geophysical Research: Planets* 127: e2021JE006916.

Condit, R. H., Hobbins, R. R., and Birchenall, C. E. 1974. Self-Diffusion of Iron and Sulfur in Ferrous Sulfide. *Oxidation of Metals* 8: 409–455.

Delbo, M., Libourel, G., Wilkerson, J., Murdoch, N., Michel, P., Ramesh, K. T., Ganino, C., Verati, C., and Marchi, S. 2014. Thermal Fatigue as the Origin of Regolith on Small Asteroids. *Nature* 508: 233–36.

Foley, C. N., Nittler, L. R., McCoy, T. J., Lim, L. F., Brown, M. R. M., Starr, R. D., and Trombka, J. I. 2006. Minor Element Evidence that Asteroid 433 Eros is a Space-Weathered Ordinary Chondrite Parent Body. *Icarus* 184: 338–343.

Gladman, B. J., Migliorini, F., Morbidelli, A., Zappalà, V., Michel, P., Cellino, A., Froeschlé, C., Levison, H. F., Bailey, M., and Duncan, M. 1997. Dynamical Lifetimes of Objects Injected into Asteroid Belt Resonances. *Science* 277: 197–201.

Granvik, M., Morbidelli, A., Jedicke, R., Bolin, B., Bottke, W. F., Beshore, E., Vokrouhlický, D., Nesvorný, D., and Michel, P. 2018. Debiased Orbit and Absolute-Magnitude Distributions for near-Earth Objects. *Icarus* 312: 181–207.

Greenwood, R. C., Franchi, I. A., Findlay, R., Malley, J. A., Ito, M., Yamaguchi, A., Kimura, M., et al. 2023. Oxygen Isotope Evidence from Ryugu Samples for Early Water Delivery to Earth by CI Chondrites. *Nature Astronomy* 7: 29–38.

Harries, D., and Langenhorst, F. 2013. The Nanoscale Mineralogy of Fe, Ni Sulfides in Pristine and Metamorphosed CM and CM/CI-Like Chondrites: Tapping a Petrogenetic Record. *Meteoritics and Planetary Science* 48: 879–903.

Harries, D., Pollok, K., and Langenhorst, F. 2011. Translation Interface Modulation in NC-Pyrrhotites: Direct Imaging by TEM and a Model toward Understanding Partially Disordered Structural States. *American Mineralogist* 96: 716–731.

Harries, D., Pollok, K., and Langenhorst, F. 2013. Oxidative Dissolution of 4C- and NC-Pyrrhotite: Intrinsic Reactivity Differences, pH Dependence, and the Effect of Anisotropy. *Geochimica et Cosmochimica Acta* 102: 23–44.

Herbert, F. W., Krishnamoorthy, A., Rands, L., Vliet, K. J. V., and Yildiz, B. 2015. Magnetic Diffusion Anomaly at the Néel Temperature of Pyrrhotite, $Fe_{1-x}S$. *Physical Chemistry Chemical Physics* 17: 11036–41.

Housen, K. R., Wilkening, L. L., Chapman, C. R., and Greenberg, R. 1979. Asteroidal Regoliths. *Icarus* 39: 317–351.

Izaola, Z., Gonzalez, S., Elcoro, L., Perez-Mato, J. M., Madariaga, G., and Garcia, A. 2007. Revision of Pyrrhotite Structures within a Common Superspace Model. *Acta Crystallographica Section B: Structural Science* 63: 693–702.

Jewitt, D., Weaver, H., Agarwal, J., Mutchler, M., and Drahus, M. 2010. A Recent Disruption of the Main-Belt Asteroid P/2010 A2. *Nature* 467: 817–19.

Jin, L., Koulialias, D., Schnedler, M., Gehring, A. U., Pósfai, M., Ebert, P., Charilaou, M., et al. 2021. Atomic-Scale Characterization of Commensurate and Incommensurate Vacancy Superstructures in Natural Pyrrhotites. *American Mineralogist* 106: 82–96.

Kaasalainen, M., Ďurech, J., Warner, B. D., Krugly, Y. N., and Gaftonyuk, N. M. 2007. Acceleration of the Rotation of Asteroid 1862 Apollo by Radiation Torques. *Nature* 446: 420–22.

Kracher, A., and Sears, D. W. G. 2005. Space Weathering and the Low Sulfur Abundance of Eros. *Icarus* 174: 36–45.

Langenhorst, F., Harries, D., Pollok, K., and van Aken, P. A. 2014. Mineralogy and Defect Microstructure of an Olivine-Dominated Itokawa Dust Particle: Evidence for Shock Metamorphism, Collisional Fragmentation, and LL Chondrite Origin. *Earth, Planets and Space* 66: 118.

Loeffler, M. J., Dukes, C. A., Chang, W. Y., McFadden, L. A., and Baragiola, R. A. 2008. Laboratory Simulations of Sulfur Depletion at Eros. *Icarus* 195: 622–29.

Lowry, S. C., Fitzsimmons, A., Pravec, P., Vokrouhlický, D., Boehnhardt, H., Taylor, P. A., Margot, J. L., et al. 2007. Direct Detection of the Asteroidal YORP Effect. *Science* 316: 272–74.

Mang, C., Kontny, A., Harries, D., Langenhorst, F., and Hecht, L. 2012. Iron Deficiency in Pyrrhotite of Suevites

from the Chesapeake Bay Impact Crater, USA—A Consequence of Shock Metamorphism? *Meteoritics & Planetary Science* 47: 277–295.

Matsumoto, T., Harries, D., Langenhorst, F., Miyake, A., and Noguchi, T. 2020. Iron Whiskers on Asteroid Itokawa Indicate Sulfide Destruction by Space Weathering. *Nature Communications* 11: 1117.

Matsumoto, T., Noguchi, T., Miyake, A., Igami, Y., Haruta, M., Saito, H., Hata, S., et al. 2022. Space Weathering of Anhydrous Minerals in Regolith Samples from the C-Type Asteroid Ryugu. *53rd Lunar and Planetary Science Conference*, abstract 1693.

Matsumoto, T., Noguchi, T., Tobimatsu, Y., Harries, D., Langenhorst, F., Miyake, A., and Hidaka, H. 2021. Space Weathering of Iron Sulfides in the Lunar Surface Environment. *Geochimica et Cosmochimica Acta* 299: 69–84.

Michel, P., and Delbo, M. 2010. Orbital and Thermal Evolutions of Four Potential Targets for a Sample Return Space Mission to a Primitive Near-Earth Asteroid. *Icarus* 209: 520–534.

Michel, P., Froeschle, C., and Farinella, P. 1996. Dynamical Evolution of Two near-Earth Asteroids to be Explored by Spacecraft: (433) Eros and (4660) Nereus. *Astronomy and Astrophysics* 313: 993–1007.

Michel, P., and Yoshikawa, M. 2005. Earth Impact Probability of the Asteroid (25143) Itokawa to be Sampled by the Spacecraft Hayabusa. *Icarus* 179: 291–96.

Morimoto, N., Gyobu, A., Mukaiyama, H., and Izawa, E. 1975. Crystallography and Stability of Pyrrhotites. *Economic Geology* 70: 824–833.

Nakamura, T., Matsumoto, M., Amano, K., Enokido, Y., Zolensky, M. E., Mikouchi, T., Genda, H., et al. 2022. Formation and Evolution of Carbonaceous Asteroid Ryugu: Direct Evidence from Returned Samples. *Science* 379: eabn8671.

Nakato, A., Inada, S., Furuya, S., Nishimura, M., Yada, T., Abe, M., Usui, T., et al. 2022. Ryugu Particles Found outside the Hayabusa2 Sample Container. *Geochemical Journal* 56: 197–222.

Nakato, A., Yada, T., Nishimura, M., Yogata, K., Miyazaki, A., Nagashima, K., Hatakeda, K., et al. 2023. Variations of the Surface Characteristics of Ryugu Returned Samples. *Earth, Planets and Space* 75: 45.

Nakazawa, H., and Morimoto, N. 1971. Phase Relations and Superstructures of Pyrrhotite, $Fe_{1-x}S$. *Materials Research Bulletin* 6: 345–357.

Nittler, L. R., Starr, R. D., Lim, L., Mccoy, T. J., Burbine, T. H., Reedy, R. C., Trombka, J. I., et al. 2001. X-Ray Fluorescence Measurements of the Surface Elemental Composition of Asteroid 433 Eros. *Meteoritics & Planetary Science* 36: 1673–95.

Noguchi, T., Matsumoto, T., Miyake, A., Igami, Y., Haruta, M., Saito, H., Hata, S., et al. 2023. A Dehydrated Space-Weathered Skin Cloaking the Hydrated Interior of Ryugu. *Nature Astronomy* 7: 170–181.

Noguchi, T., Nakamura, T., Kimura, M., Zolensky, M. E., Tanaka, M., Hashimoto, T., Konno, M., et al. 2011. Incipient Space Weathering Observed on the Surface of Itokawa Dust Particles. *Science* 333: 1121–25.

Okazaki, R., Marty, B., Busemann, H., Hashizume, K., Gilmour, J. D., Meshik, A., Yada, T., et al. 2022. Noble Gases and Nitrogen in Samples of Asteroid Ryugu Record its Volatile Sources and Recent Surface Evolution. *Science* 379: eabo0431.

Öpik, E. J. 1951. Collision Probabilities with the Planets and the Distribution of Interplanetary Matter. *Proceedings of the Royal Irish Academy. Section A: Mathematical and Physical Sciences* 54: 165–199.

Pebesma, E. J. 2004. Multivariable Geostatistics in S: The gstat Package. *Computers & Geosciences* 30: 683–691.

Pieters, C. M., and Noble, S. K. 2016. Space Weathering on Airless Bodies. *Journal of Geophysical Research: Planets* 121: 2016JE005128.

Pieters, C. M., Taylor, L. A., Noble, S. K., Keller, L. P., Hapke, B., Morris, R. V., Allen, C. C., McKay, D. S., and Wentworth, S. 2000. Space Weathering on Airless Bodies: Resolving a Mystery with Lunar Samples. *Meteoritics & Planetary Science* 35: 1101–7.

Powell, A. V., Vaqueiro, P., Knight, K. S., Chapon, L. C., and Sanchez, R. D. 2004. Structure and Magnetism in Synthetic Pyrrhotite Fe_7S_8: A Powder Neutron-Diffraction Study. *Physical Review B* 70: 014415.

Rau, H. 1976. Energetics of Defect Formation and Interaction in Pyrrhotite $Fe_{1-x}S$ and its Homogeneity Range. *Journal of Physics and Chemistry of Solids* 37: 425–29.

Rubincam, D. P. 2000. Radiative Spin-Up and Spin-Down of Small Asteroids. *Icarus* 148: 2–11.

Schrader, D. L., Davidson, J., McCoy, T. J., Zega, T. J., Russell, S. S., Domanik, K. J., and King, A. J. 2021. The Fe/S Ratio of Pyrrhotite Group Sulfides in Chondrites: An Indicator of Oxidation and Implications for Return Samples from Asteroids Ryugu and Bennu. *Geochimica et Cosmochimica Acta* 303: 66–91.

Shimaki, Y., Senshu, H., Sakatani, N., Okada, T., Fukuhara, T., Tanaka, S., Taguchi, M., et al. 2020. Thermophysical Properties of the Surface of Asteroid 162173 Ryugu: Infrared Observations and Thermal Inertia Mapping. *Icarus* 348: 113835.

Singerling, S. A., and Brearley, A. J. 2018. Primary Iron Sulfides in CM and CR Carbonaceous Chondrites: Insights into Nebular Processes. *Meteoritics & Planetary Science* 53: 2078–2106.

Skála, R., Cisařová, I., and Drábek, M. 2006. Inversion Twinning in Troilite. *American Mineralogist* 91: 917–921.

Tachibana, S., Sawada, H., Okazaki, R., Takano, Y., Sakamoto, K., Miura, Y. N., Okamoto, C., et al. 2022. Pebbles and Sand on Asteroid (162173) Ryugu: In Situ Observation and Particles Returned to Earth. *Science* 375: 1011–16.

Tachibana, S., and Tsuchiyama, A. 1998. Incongruent Evaporation of Troilite (FeS) in the Primordial Solar Nebula: An Experimental Study. *Geochimica et Cosmochimica Acta* 62: 2005–22.

Taylor, P. A., Margot, J. L., Vokrouhlický, D., Scheeres, D. J., Pravec, P., Lowry, S. C., Fitzsimmons, A., et al. 2007. Spin Rate of Asteroid (54509) 2000 PH5 Increasing Due to the YORP Effect. *Science* 316: 274–77.

Toulmin, P., and Barton, P. B. 1964. A Thermodynamic Study of Pyrite and Pyrrhotite. *Geochimica et Cosmochimica Acta* 28: 641–671.

Tsuchiyama, A., Uyeda, C., and Makoshi, Y. 1997. Incongruent Evaporation Experiments on Iron Sulfide $(Fe_{1-\delta}S)$ under H_2-Rich (at 1 atm) and Evacuated Conditions. *Geochemical Journal* 31: 289–302.

Waldner, P., and Pelton, A. 2005. Thermodynamic Modeling of the Fe-S System. *Journal of Phase Equilibria and Diffusion* 26: 23–38.

Yada, T., Abe, M., Okada, T., Nakato, A., Yogata, K., Miyazaki, A., Hatakeda, K., et al. 2022. Preliminary

Analysis of the Hayabusa2 Samples Returned from C-Type Asteroid Ryugu. *Nature Astronomy* 6: 214–220.

Yamamoto, A., and Nakazawa, H. 1982. Modulated Structure of the NC-Type ($N = 5.5$) Pyrrhotite, $Fe_{1-x}S$. *Acta Crystallographica, Section A: Crystal Physics, Diffraction, Theoretical and General Crystallography* 38: 79–86.

Yokoyama, T., Nagashima, K., Nakai, I., Young, E. D., Abe, Y., Aléon, J., Alexander, C. M. O'D., et al. 2022. Samples Returned from the Asteroid Ryugu are Similar to Ivuna-Type Carbonaceous Meteorites. *Science* 379: eabn7850.

Zhu, C., Góbi, S., Abplanalp, M. J., Frigge, R., Gillis-Davis, J. J., and Kaiser, R. I. 2019. Space Weathering-Induced Formation of Hydrogen Sulfide (H_2S) and Hydrogen Disulfide (H_2S_2) in the Murchison Meteorite. *Journal of Geophysical Research: Planets* 124: 2772–79.

SUPPORTING INFORMATION

Additional supporting information may be found in the online version of this article.

Figure S1. Effect of different variogram models (exponential, spherical, Gaussian, wavelet) for Kriging interpolation on the obtained diffusion profiles.